Engineering Analysis with Boundary Elements 123 (2021) 93–106

Contents lists available at ScienceDirect

Engineering Analysis with Boundary Elements

journal homepage: www.elsevier.com/locate/enganabound

Grout penetration process simulation and grouting parameters analysis in fractured rock mass using numerical manifold method

Xuewei Liu[a,*], Cheng Hu[a], Quansheng Liu[b], Jun He[c]

[a] State Key Laboratory of Geomechanics and Geotechnical Engineering, Institute of Rock and Soil Mechanics, Chinese Academy of Sciences, Wuhan 430071, China
[b] The key laboratory of safety for geotechnical and structural engineering of Hubei province, School of Civil Engineering, Wuhan University, Wuhan 430072, China
[c] Key Laboratory of Geotechnical Mechanics and Engineering of the Ministry of Water Resources, Changjiang River Scientific Research Institute, Wuhan, 430010, China

ARTICLE INFO

Keywords:
Numerical manifold method
Grouting
Discrete fracture networks
Rock mechanics
Propagation depth

ABSTRACT

Grouting is a commonly used technique in rock engineering to enhance the joint strength and improve the stability of surrounding rock. Grout penetration characteristic is controlled by grouting parameters and has a significant role on practice. In the study, a numerical manifold method (NMM) for grout penetration process simulation in fractured rock mass is firstly proposed. The fluid flow behaviour of the grout is assumed to be a Bingham fluid and control equations are established using discrete fracture network model. The global discretization equation, element sub-matrixes and NMM simulation algorithm for grouting are presented. Then, numerical tests for grouting process in a single fracture and a regular fracture network are conducted firstly to verify the proposed NMM grouting model by comparing with analytical solutions and experimental results. Furthermore, the effects of mesh size, fracture and slurry parameters on the grouting performance are systematically investigated using a random fracture network example. The numerical results indicate that the grouted zone and propagation depth decrease as the mesh size of numerical model and yield strength increases, while it increases as initial fracture aperture and grouting pressure increases.

1. Introduction

The existence of fractures can decrease rock mass strength and form flowing channels, which may cause an instability and groundwater gush in the surrounding rock [1,2]. A grouting method, as an effective technique to improve the mechanical properties of rocks and prevent groundwater leakage, is widely used in deep mining, civil and petroleum reservoir engineering [3]. Many grouting parameters, such as initial pressure, and slurry gel time can control the grouting projects effectively. Therefore, grouting process and influence factors should be investigated.

Many methods, such as laboratory tests, analytical analysis, and numerical simulation, have been proposed to investigate the grouting process. It is known that both experimental and analytical methods have some limitations to obtain required precision [4]. Considering the economics and practicality, numerical methods are a preferred way to study slurry migration process in fractured rock mass. For example, Baca *et al.* [5] modelled fluid flow in fractured porous rock masses by finite element method (FEM) and Prevost and Sukumar [6] used extended FEM to study the grouting process in three-dimensional reservoir. However, these two techniques are continuum-based methods and the definition of equivalent permeability was used to describe the fluid flowing in fractured rock mass. Furthermore, many discontinuum-based methods were proposed on basis of discrete fractures networks (DFN) model. Saeidi *et al.* [7] propose a numerical model to predict grout flow and penetration length into the jointed rock mass using discrete element method (DEM) and the effect of rock mass properties on grout flow rate and penetration length were fully investigated. Eriksson *et al.* [8] predicted grout spread in a two-dimensional lattice network using DEM. Xiao *et al.* [9] developed a grouting module based on the discontinuous deformation analysis (DDA) and studied the transient flow of grout. However, the above studies only investigated the grout penetration in regular fracture networks, which is fracture network with two sets of symmetrical or perpendicular fractures.

Grouting is a process of slurry migration into random fracture network. Mohajerani *et al.* [10] proposed an efficient algorithm for simulating grouting process and developed a code to track the paths of grout propagation in discrete fracture networks. Liu *et al.* [11,12] and Sun *et al.* [13] developed a combined finite-discrete element method grouting model to study the effect of in-situ stress conditions on grout penetration in fracture network. However, in DEM and finite-discrete element method (FEDM) model, meshes can only along the cracks' boundaries.

Numerical manifold method (NMM), as a method combining the FEM and discontinuous deformation analysis (DDA), has two indepen-

* Corresponding author.
E-mail address: liuxw87@126.com (X. Liu).

https://doi.org/10.1016/j.enganabound.2020.11.008
Received 17 September 2020; Received in revised form 15 November 2020; Accepted 16 November 2020
Available online 3 December 2020

dent cover systems and can generate meshes without considering the cracks. The NMM has been applied in rock dynamics [14–16], rock failure processes [17], thermal shock cracking [18,19], and rock creep [20]. Over the past decades, the NMM has also been explored in many other fields [21–32]. Hu and Rutqvist [33] simulated the dynamic contact evolution at the microscale for realistic geomaterials having arbitrary shapes of grains and interfaces by NMM. Wu *et al.* [34] proposed a micro-mechanical NMM modeling and then investigated macro-mechanical response and fracture behavior of rock. Hu and Rutqvist [35] developed an approach for coupled processes in fractured geological media based NMM at multiple scales.

Application of NMM for fluid flow in porous or fractured media has also been developed in recent years. Zheng *et al.* [36] investigated unconfined seepage flow in porous media using NMM. Yang *et al.* [21] adopted NMM to model fluid flow through fractures and hydraulic fracturing process under coupled hydro-mechanical. Hu *et al.* [37,38] proposed a new model for simulation of fluid flow and coupled hydro-mechanical process in fractured rock mass. Ma *et al.* [39,40] developed an NMM model for analysis of two-phase fluid flow in fracture networks. However, application of NMM to the penetration process of grout in fractured rock mass is less studied.

In this paper, the grout fluid flowing behaviour is supposed as a Bingham fluid and discrete fracture networks model is used to develop the NMM grouting model. The NMM is extended to simulate the grout penetration in fractured rock mass. The discretization equations and NMM algorithm for grouting are firstly presented. Then the proposed NMM grouting model is verified by comparing with analytical solutions or experimental results. Finally, influence factors on grout propagation depth are investigated by the proposed model.

2. Basic theory of NMM

In NMM, there are two independent cover systems, including mathematical cover (MC) and physical cover (PC). The manifold element (ME) can generate from these two cover systems. The MCs are a set of overlapped patches and they do not need to be consistent with but should be larger than the problem domain. The PC patches are the intersection of MCs and the problem domain and union of all the PC patches is PC system. Then, the ME is generated by the intersection of different overlapped PC patches.

To describe the local field characteristic, local approximation functions (or cover functions), which can be constant basis, linear basis, or higher-order polynomial functions, are defined on each PCs. The polynomial function can be expressed as:

$$S_C = r(x,y) = \left\{1, x, y, \cdots x^n, x^{n-1}y \cdots xy^{n-1}, y^n\right\} \quad (n = 0, 1, 2 \cdots) \tag{1}$$

Therefore, the local field characteristic that is defined on each PC patch can be expressed as:

$$g_i(x) = R^T(x) \cdot D \tag{2}$$

where D is the degrees of freedom and R^T is polynomial basis, which can be given as follows for two-dimensional problems:

$$R^T(x) = \begin{bmatrix} 1 & 0 & x & 0 & y & 0 & \cdots \\ 0 & 1 & 0 & x & 0 & y & \cdots \end{bmatrix} \tag{3}$$

Further, weight functions, which are defined by the MC, are used to connect the local approximation displacement function (listed in Eq. (2)) together and form global displacement function over any ME. The relationship between local approximation displacement function and global displacement function can be expressed as follows by weight functions:

$$G(x) = \sum_i w_i(x) \cdot g_i(x) \tag{4}$$

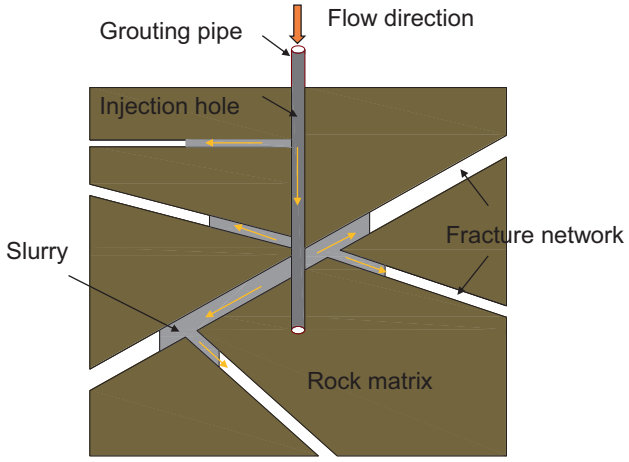

Fig. 1. Illustration of grouting process model in fractured rock mass.

where $w_i(x)$ is the weight function for each MC patch, which should satisfy the following conditions:

$$\begin{cases} w_i(x) \geq 0 \forall (x) \in M_i \\ w_i(x) = 0 \forall (x) \notin M_i \end{cases} \tag{5}$$

with

$$\sum_{(x) \in M_i} w_i(x) = 1 \tag{6}$$

Generally, the MC parches can be arbitrary shape. In this work, triangular meshes are adopted to generate MCs. Therefore, the weight function of NMM is same as that of 3-node finite element. Besides, the polynomial basis in Eq. (3) is set as constant to avoid the linear dependence problem. On basis of them, the global governing equations can be expressed as follows [26]:

$$K D = F \tag{7}$$

3. Grout penetration simulation using NMM

Rock fracture grouting process model is shown in Fig. 1. From Fig. 1, the slurry travels from grouting pipe to injection hole and then injects into the joints under the initial grouting pressure. Fractured rock mass consists of both fracture and rock matrix. Therefore, in this work, some assumptions are introduced as follows: 1) The slurry flow is only occurred in the fracture networks and slurry entered the rock matrix can be ignored during the grouting process; 2) The slurry is incompressible and homogeneous fluid; 3) The slurry pattern and density remains unchanged during grouting.

3.1. Bingham flow equations

The slurry used in geotechnical engineering is a mixture of cement and water, when ratio of water to cement varies from 0.6 to 1.0, the slurry has plastic yield strength and viscosity [42]. Since the viscosity of the grout is usually high, the slurry flow behavior can be supposed as a Bingham fluid [43,44], with the following rheological equations [41]:

$$\tau = \tau_0 + \mu(-dv/dy) \tag{8}$$

where τ is shear strength, τ_0 is yield strength, μ is grout dynamic viscosity, v is the slurry flow velocity, and y is distance in perpendicular to grout flow direction.

Fig. 2 shows a Bingham grout fluid model in a plate fracture. Due to the yield strength of the grout, a plug region (the yellow area) with same velocity exists in the middle of slurry and flows together. Outside the plug region is the grout fluid with velocity gradient. Therefore, the

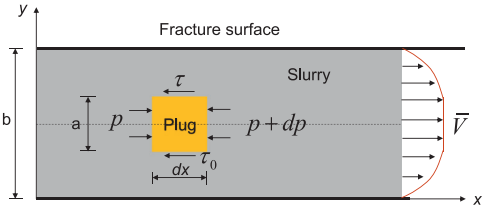

Fig. 2. Bingham grout fluid model in a plate fracture.

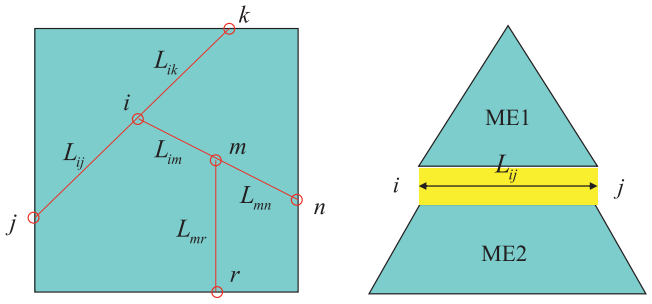

Fig. 3. Relation between fracture networks and manifold element. (a) Fracture networks. (b) Manifold elements on a crack.

shear strength in the plug area keeps as τ_0 from Eq. (8) and the height of plug can be obtained by equilibrium equation:

$$a = \frac{2\tau_0}{-(dp/dx)} \tag{9}$$

where a is plug height and p is grout pressure. Considering that the plug height must be smaller than fracture aperture, which can be expressed as follows:

$$\frac{2\tau_0}{b} \le -\frac{dp}{dx} \tag{10}$$

where b is fracture aperture. Eq. (10) indicates that there is a critical pressure gradient for Bingham grout fluid, which can be defined as:

$$\lambda_0 = \frac{2\tau_0}{b} \tag{11}$$

where λ_0 is critical pressure gradient. When pressure gradient is no less than λ_0, the fluid can flow, otherwise it will stop flowing.

From Fig. 2, it is clearly that the Bingham grout fluid velocity is varying in fracture height direction. According to the grout flow governing differential equations and boundary conditions [11], the average grout flow velocity can be expressed as follows:

$$\bar{V} = \frac{b^2}{12\mu}\left(-\frac{dp}{dx}\right)\left[1 - \frac{3\tau_0}{b(-dp/dx)} + \frac{4{\tau_0}^3}{b^3(-dp/dx)^3}\right] \tag{12}$$

Then, the grout flow rate per unit time can be obtained by:

$$q = \bar{V}\cdot b = \frac{b^3}{12\mu}\left[-\frac{dp}{dx} - \frac{3\tau_0}{b} + \frac{4{\tau_0}^3}{b^3(-dp/dx)^2}\right] \tag{13}$$

3.2. Fluid pressure

In this study, grout fluid flow is calculated through discrete fracture network model (DFN), as shown in Fig. 1. The key to solve DFN model is to obtain the intersection and fracture line of fracture network. The intersection is obtained from geometrical relationship of fracture network and can be defined as hydraulic node during calculation, while fracture line is formed by two adjacent hydraulic nodes and can be defined as hydraulic line element in NMM. As shown in Fig. 3 (a), there are 3 cracks in a square domain and then generate 6 hydraulic nodes (red circles) and 5 hydraulic line element (such as L_{ik} *et al.*).

Because the fracture networks connect each other, the mathematical covers will be split by cracks and then forms different manifold elements on either side of the crack. As shown in Fig. 3(b), two MEs, namely ME1 and ME2 on the hydraulic line element L_{ij}, were generated and two hydraulic nodes (i and j) are connected by L_{ij}. Based on Eq. (13), the grout flow rate from node i to j through L_{ij} can be calculated as:

$$q_{ij} = \frac{{b_{ij}}^3}{12\mu}\left[-\frac{\Delta p_{ij}}{l_{ij}} - \frac{3\tau_0}{b_{ij}} + \frac{4{\tau_0}^3}{{b_{ij}}^3\left(-\Delta p_{ij}/l_{ij}\right)^2}\right] \tag{14}$$

where b_{ij}, l_{ij} and Δp_{ij} are fracture aperture, length and pressure loss of hydraulic line element L_{ij}, respectively. The pressure loss between node i and j can be defined as:

$$\Delta p_{ij} = p_i - p_j + \rho g\left(z_i - z_j\right) \tag{15}$$

where p_i and p_j are fluid pressure at hydraulic nodes i and j, respectively. Parameters z_i and z_j are vertical coordinates of hydraulic nodes i and j. ρ is fluid density.

Once the fluid pressures at each node were obtained, the load applied on manifold element edges is simplified as linear load along the hydraulic line element and the load components applied on arbitrary place (x,y) can be expressed by:

$$\begin{cases} p_x(r) = (p_{jx} - p_{ix})r + p_{ix} \\ p_y(r) = (p_{jy} - p_{iy})r + p_{iy} \end{cases} \tag{16}$$

where p_{ix} and p_{iy} stand for x-direction and y-direction load components at hydraulic node i, respectively. p_{jx} and p_{jy} stand for x-direction and y-direction load components at hydraulic node j, respectively. Parameter r is a no unit and satisfies $0 \le r \le 1$.

Therefore, the potential energy due to the fluid pressure can be expressed by:

$$\begin{aligned} \Pi_{me1} &= -\int_0^1 \begin{pmatrix} u_x(r) & u_y(r) \end{pmatrix} \begin{Bmatrix} p_x(r) \\ p_y(r) \end{Bmatrix} \cdot L_{ij}\,dr \\ &= -\left\{D_{me1}\right\}^T \int_0^1 \left[N_{me1}\begin{pmatrix} x(r) & y(r) \end{pmatrix}\right]^T \cdot \begin{Bmatrix} p_x(r) \\ p_y(r) \end{Bmatrix} \cdot L_{ij}\,dr \end{aligned} \tag{17}$$

where D_{me1} and N_{me1} are DOFs and weight function of manifold element ME1, respectively. x(r) and y(r) are x-direction and y-direction coordinates of arbitrary point on edge 1–2 and can be obtained by:

$$\begin{cases} x(r) = (x_j - x_i)r + x_i \\ y(r) = (y_j - y_i)r + y_i \end{cases} \tag{18}$$

From Eq. (17), the load vector formed by fluid pressure can be obtained by:

$$F_{me1} = L_{ij}\int_0^1 \left[N_{me1}\begin{pmatrix} x(r) & y(r) \end{pmatrix}\right]^T \cdot \begin{Bmatrix} p_x(r) \\ p_y(r) \end{Bmatrix} dr \tag{19}$$

3.3. NMM simulation algorithm

It is known that the total volume of grout flow into and out a hydraulic node is equal to the volume change of grout fluid, which can be expressed as [41]:

$$\left(\sum_{k=1}^{m} q_k\right)_i + Q_i = -\frac{1}{2}\alpha_i \sum_{k=1}^{m} b_k l_k \frac{dp_i}{dt} (i = 1 \cdots N) \tag{20}$$

where q_k, b_k, and l_k are the grout fluid rate, fracture aperture, and length of the k^{th} hydraulic line element connected with hydraulic node i, respectively. The parameter n is the total number of hydraulic line elements that connected with hydraulic node i and N is the total number of hydraulic nodes. Parameters Q_i, α_i, and p_i are grout fluid source sink term, elastic storage coefficient, and fluid pressure, respectively.

For the hydraulic node 1, as shown in Fig. 4, there are 3 hydraulic line elements L_{12}, L_{13}, and L_{14}. Therefore, Eq. (20) can be rewritten as:

$$\sum_{k=2}^{4} q_{1k} + Q_1 = \frac{1}{2}\alpha_1 \sum_{k=2}^{4} b_k l_k \frac{dp_1}{dt} \tag{21}$$

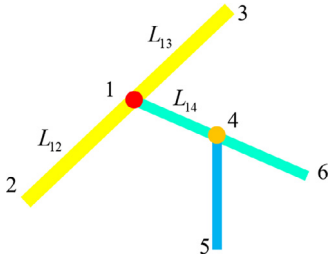

Fig. 4. A simplified fracture network.

From Eq. (14), the Bingham grout fluid rate can be obtained as:

$$q_{1k} = \frac{{b_{1k}}^3}{12\mu}\left[-\frac{\Delta p_{1k}}{l_{1k}} - \frac{3\tau_0}{b_{1k}} + \frac{4{\tau_0}^3}{{b_{1k}}^3\left(-\Delta p_{1k}/l_{1k}\right)^2}\right] \tag{22}$$

Generally, the higher-order small term in Eq. (22) can be ignored and this equation can be simplified as:

$$q_{1k} = \frac{{b_{1k}}^3}{12\mu}\left[-\frac{p_1}{l_{1k}} + \frac{p_k}{l_{1k}} - \frac{3\tau_0}{b_{1k}}\right] \tag{23}$$

Substituting Eq. (23) to Eq. (21) and it becomes:

$$\sum_{k=2}^{4}\left(\frac{{b_{1k}}^3}{12\mu}\left[-\frac{p_1}{l_{1k}} + \frac{p_k}{l_{1k}} - \frac{3\tau_0}{b_{1k}}\right]\right) + Q_1 = \frac{1}{2}\alpha_1\sum_{k=2}^{4} b_k l_k \frac{dp_1}{dt} \tag{24}$$

Decomposing Eq. (24), the discretization equation for grout fluid can be expressed as:

$$M_1 \cdot p - T_1 + Q_1 = S_1\frac{dp_0}{dt} \tag{25}$$

where

$$M_1 = \left[\ -\sum_{k=2}^{4}\left(\frac{{b_{1k}}^3}{12\mu\cdot l_{1k}}\right) \quad \frac{{b_{12}}^3}{12\mu\cdot l_{12}} \quad \frac{{b_{13}}^3}{12\mu\cdot l_{13}} \quad \frac{{b_{14}}^3}{12\mu\cdot l_{14}}\ \right] \tag{26}$$

$$T_1 = \sum_{k=2}^{4}\left(\frac{\tau_0\cdot {b_{1k}}^2}{4\mu\cdot l_{1k}}\right) \tag{27}$$

$$S_1 = \left[\ \frac{1}{2}\alpha_1\sum_{k=2}^{4} b_k l_k \quad 0 \quad 0 \quad 0\ \right] \tag{28}$$

$$p_0 = \left[\ p_1 \quad p_2 \quad p_3 \quad p_4\ \right]^T \tag{29}$$

The fluid pressure derivative to time in Eq. (25) can be expressed as:

$$\frac{dp}{dt} = \frac{{p_0}^{n+1} - {p_0}^n}{\Delta t} \tag{30}$$

where ${p_0}^{n+1}$, ${p_0}^n$ are the pressure at time step n+1 and time step n, respectively. Δt is time step. Substituting Eq. (30) to Eq. (25), element discretization equation can be expressed as:

$$\left(M_1 - \frac{S_1}{\Delta t}\right)\cdot {p_0}^{n+1} = T_1 - Q_1 - \frac{S_1}{\Delta t}\cdot {p_0}^n \tag{31}$$

Combining all the element discretization equations together, the corresponding global discretization equation can be obtained as:

$$K\cdot p^{n+1} = F \tag{32}$$

where

$$K = M - \frac{S}{\Delta t} \tag{33}$$

$$F = T - Q - \frac{S}{\Delta t}\cdot p^n \tag{34}$$

And the sub-matrixes for Eq. (33) and Eq. (34) can be calculated by:

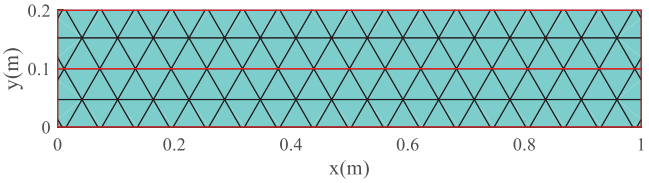

Fig. 5. Calculation model and numerical meshes of example 2.

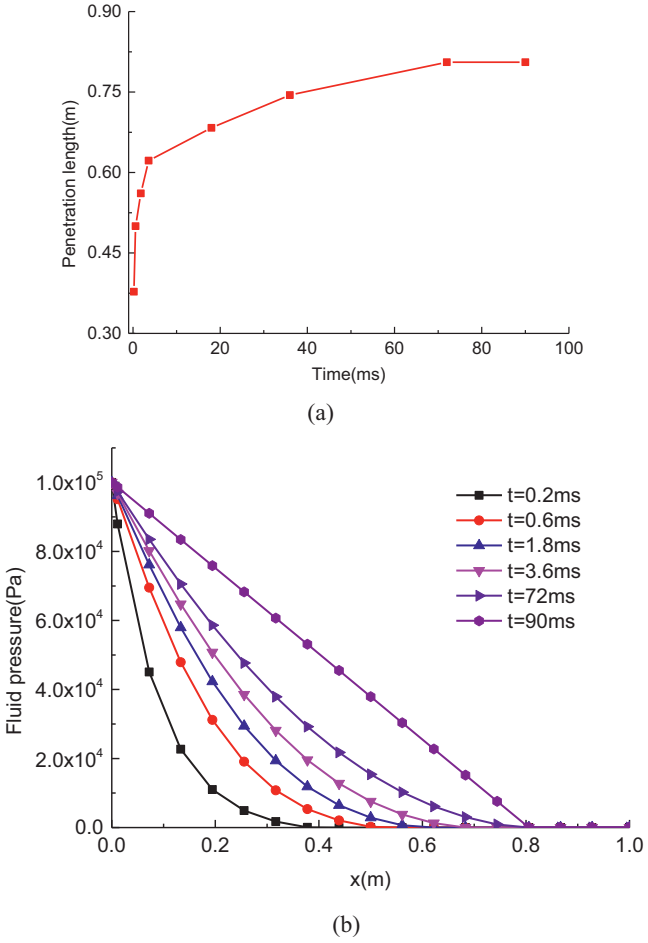

Fig. 6. Numerical results. (a) Relationship between numerical penetration length and time. (b) Grout fluid pressure distribution at different time.

$$\begin{cases} M(i,i) = -\sum_{k=1}^{m}\left(\frac{{b_{ik}}^3}{12\mu\cdot l_{ik}}\right) \\ M(i,j) = 0 nodes i and j are not connected \\ M(i,j) = \frac{{b_{ij}}^3}{12\mu\cdot l_{ij}} nodes i and j are connected \end{cases} \tag{35}$$

$$\begin{cases} S(i,i) = \frac{1}{2}\alpha_i\sum_{k=1}^{m} b_k l_k \\ S(i,j) = 0 i \neq j \end{cases} \tag{36}$$

$$T(i,1) = \sum_{k=1}^{m}\left(\frac{\tau_0\cdot {b_{ik}}^2}{4\mu\cdot l_{ik}}\right) \tag{37}$$

$$Q(i,1) = Q_i \tag{38}$$

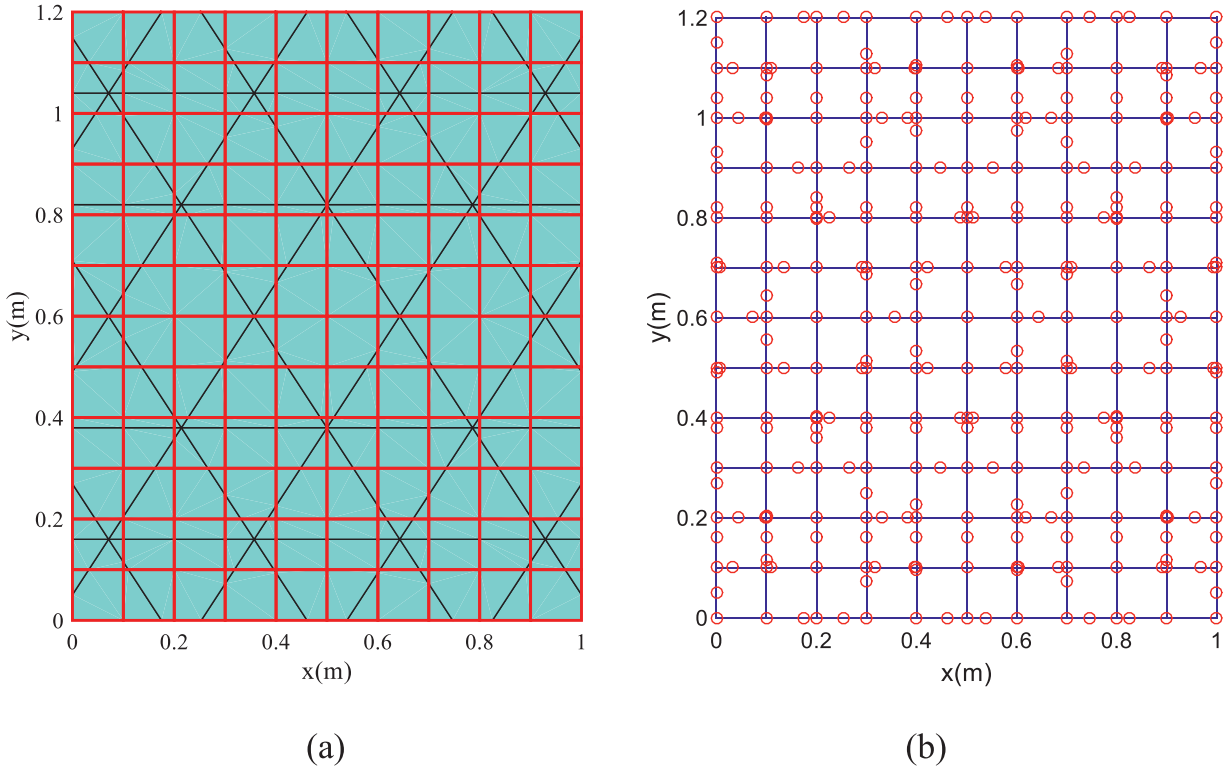

Fig. 7. Computational model. (a) Numerical meshes. (b) Hydraulic nodes and line elements.

$$p^n=\begin{bmatrix} p_1{}^n & p_2{}^n & \cdots & p_{N-1}{}^n & p_N{}^n \end{bmatrix}^T \tag{39}$$

where $i, j = 1, 2, \ldots N$.

Before the numerical calculation, information of hydraulic nodes and line element should be first obtained. During the generation process of PCs and MEs, information of hydraulic line elements, including serial number of this line and end nodes, can be easily searched out by comparing the positions of edges of MEs and discontinuous boundaries. Information of a specific node includes the serial numbers of connected hydraulic line elements and adjacent hydraulic nodes, which also can be found by meshing process.

After that, grout fluid pressure can be calculated by Eq. (32) – Eq. (39). The numerical manifold method simulation algorithm includes following steps:

(1) Mesh generation and NMM data and boundary conditions should be first conducted.
(2) Assign initial grouting pressures p^0 for calculation. The grouting pressures are zero on all the hydraulic nodes except injection points.
(3) Inherit grout fluid pressure p^n from last time step n.

(3.1) Solve the Eq. (32) – Eq. (39) to obtain grout fluid pressure p^{n+1} on each hydraulic nodes.
(3.2) Calculate the sub-matrixes including stiffness, body force etc. by NMM.
(3.3) Calculate the sub-matrixes induced by grout fluid pressure p^{n+1} by Eq. (19).
(3.4) Take the sub-matrixes into global matrix and solve the global equations.

(4) Compare the calculated and critical pressure gradient in (11).

(4.1) If the calculated pressure gradient is no less than λ_0, the fluid can flow and go to next time step
(4.2) otherwise it will stop flowing.

(5) Update the sub-matrixes in Eq. (32) – Eq. (39) and enter into next time step until simulation completed.

4. Validation of proposed method

Two numerical tests, including grouting in a single fracture and a regular fracture network, are conducted in the section to verify the proposed NMM grouting method by comparing with numerical results and that of analytical or experimental results.

4.1. Grouting in a single fracture

A rock sample with a single through crack is then simulated. As shown in Fig. 5, the rock sample is a rectangle with length of 1 m and height 0.2 m. Coordinates of the pre-existing crack endpoints are (0, 0.1 m) and (1 m, 0.1 m), respectively. A grout slurry keeps injecting into the crack at the injection point (0, 0.1 m) with a constant grouting pressure P_0=0.1 MPa. The right side is fixed and impermeable. Mechanical parameters are same as those used in section 4.1. The Bingham grout fluid parameters are: the viscosity is 0.001 Pa s, and yield strength is 10 Pa.

According to Eq. (11), the analytical solution for grout penetration length in this test can be calculated by:

$$L=\frac{P_0 b}{2\tau_0}=0.8m \tag{40}$$

Fig. 6 (a) shows the relationship between numerical penetration length and time. It can be found that the penetration length increases from 0.3778 m to 0.8056 m as time increases from 0.2 ms to 90 ms. From Fig. 10 (a), it is also clear that the penetration length keeps constant when time reaches 76 ms, which is in good accordance with the analytical result. Furthermore, as shown in Fig. 6 (b), the grout fluid pressure distribution at different time has also been discussed. With increase of calculation time, the grout flows from injection point to the

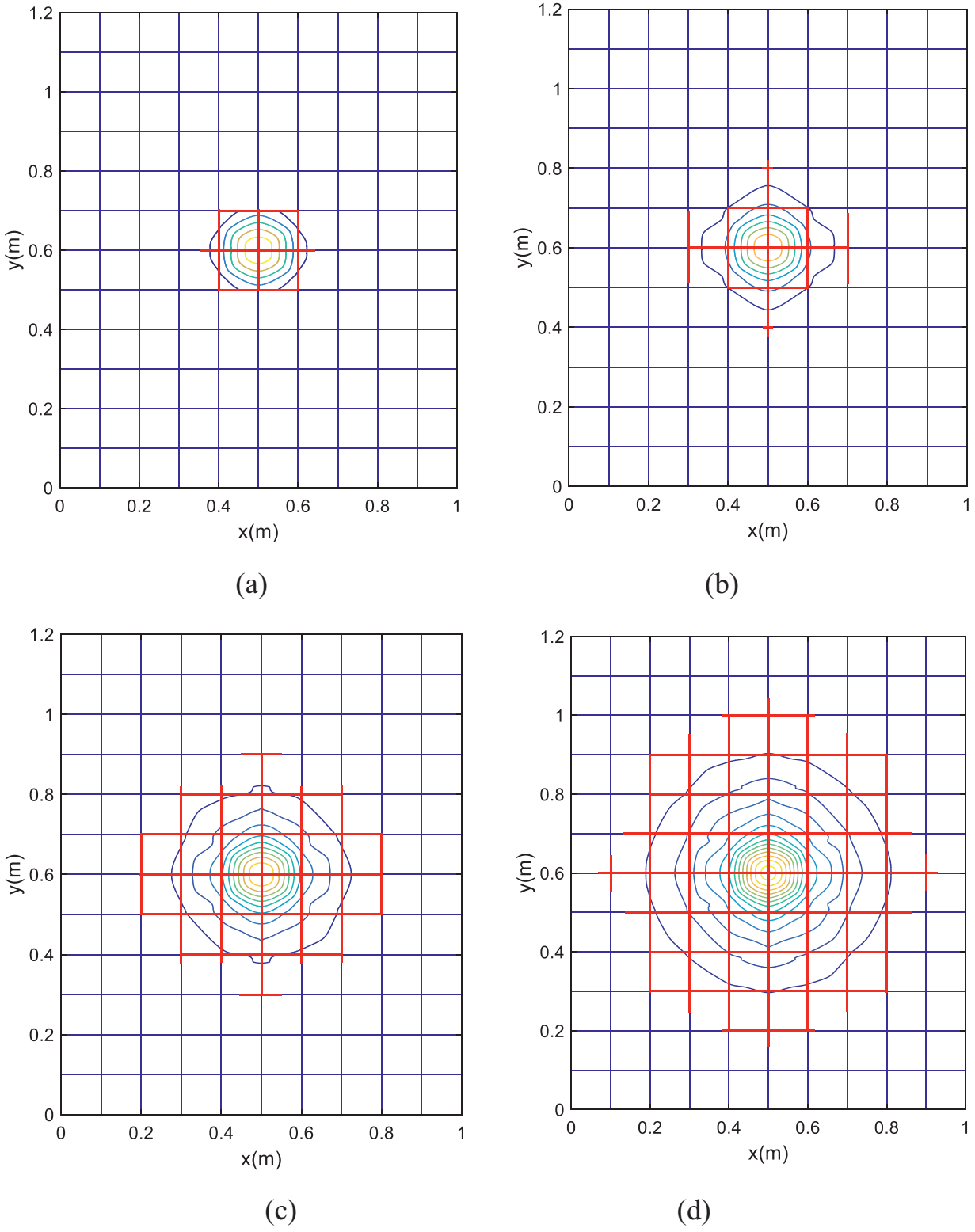

Fig. 8. Numerical calculation results of grouting process at different time step. (a) 2.5 s. (b) 6 s. (c) 22 s. (d) 65 s.

crack gradually and fluid pressure increases, too. Besides, the fluid pressure distribution along the crack is nonlinear first and finally it will be linear. As a result, the final pressure gradient at everywhere in the crack is equal to the critical value at the steady-state, which agrees well with the results of Sun *et al.* [12]. The results observed in this example verified the effectively of grout fluid flow simulation in a single fracture by proposed NMM grouting method.

4.2. Grouting in a regular fracture network

In this section, a regular fracture network example, which was an experimental test conducted by Hakansson [45] and has been widely used as a comparison of numerical results [10,12], is implemented to validate the correctness of proposed NMM grouting method on grout fluid flow simulation in a complicated fracture network. As introduced

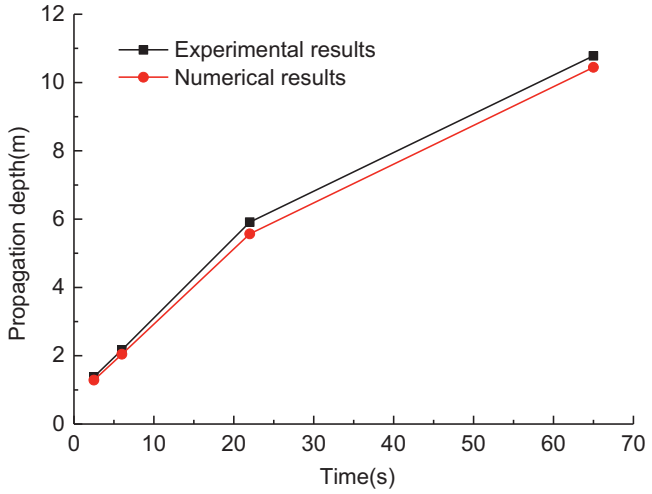

Fig. 9. Comparison of propagation depth between numerical and experimental results.

by Hakansson [45], the laboratory test used two plates of plexiglass with 1.2 m in length, 1.0 m in width and 0.015 m in height to form a lattice network with channels dimensions of 1 × 5 mm between the two plexiglasses. NMM computational model is shown in Fig. 7 (a), and the red lines is fracture networks while black line is MCs. A grout slurry keeps injecting into the crack from the injection point (0.5 m, 0.6 m) with a constant grouting pressure P_0 = 0.48 m (about 4700 Pa). The Bingham fluid parameters are 3.0 Pa in yield strength and 0.035 Pa s in viscosity. Mechanical parameters of rock mass are same as those used in section 4.1.

Numerical model includes 324 MEs and 504 PCs. Besides, there are 143 hydraulic nodes and 262 hydraulic line elements before the mesh generation. However, these two numbers increase to 331 and 450 with help of numerical manifold meshes, respectively. Fig. 7 (b) shows hydraulic nodes (red circle) and hydraulic line elements (blue line) after the mesh generation.

Fig. 8 shows the numerical calculation results at different time step. In Fig. 8, the red lines are the hydraulic line elements where the grout fluid has reached, while the remaining blue lines are grout fluid free region. Fig. 8 indicates that the grouted area increases gradually as time increases and the fluid pressure distribution at different grouting time is an approximately circle, which are consistent with the experimental results conducted by Zhang *et al.* [46]. Besides, a parameter, namely propagation depth, is defined as the total length of line elements where grout fluid arrived to evaluate the correctness of the numerical method. Fig. 9 show the comparison of propagation depth between numerical and experimental results, which shows that numerical propagation depths at different time are very close to that of experimental. The average percentage error between numerical and analytical results is 5.39% and the maximum percentage error is 6.81%. Both the comparison of grouting shape and grouting propagation depth verifies correctness of proposed NMM grouting model on grout flow simulation in fracture network.

5. Investigation the influence factors on grout propagation depth

In this section, a series of numerical tests are conducted to investigated the influence factors on grout propagation depth by a same fracture network grouting model. As shown in Fig. 10, the modeled grouting example is a rectangle with size of 3 m × 4 m. A grout injection hole (blue line) with length of 1.5 m from point (0, 2 m) to point (1.5 m, 2 m) existed in this model. Two sets of cracks are generated randomly and the angle of these two sets of cracks are set as 30°and 150°, respectively. For each set of cracks, there are 10 cracks and the crack lengths

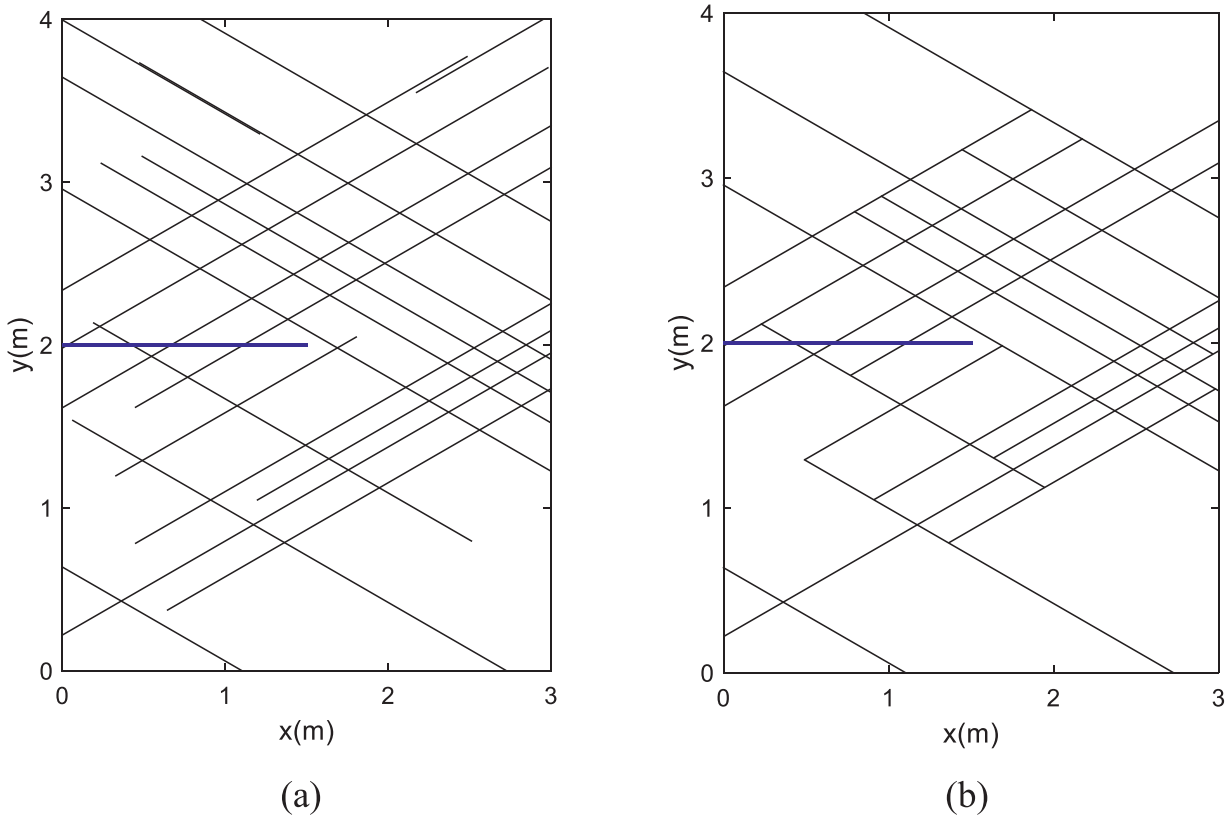

Fig. 10. The generated 2D fractured grouting model (a) Initial fracture networks (b) Simplified fracture networks.

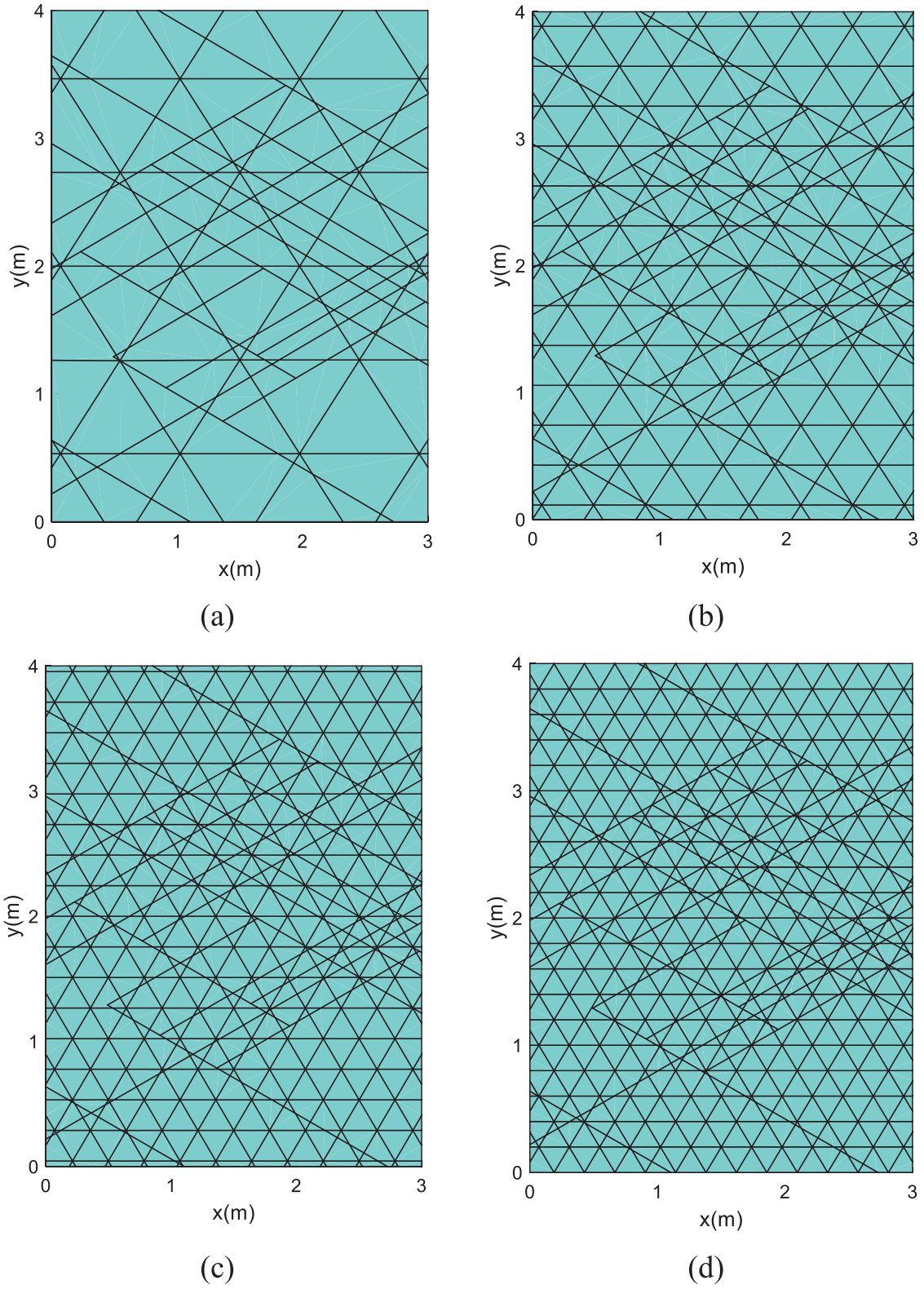

Fig. 11. Computational mesh. (a) $N_e = 216$. (b) $N_e = 544$. (c) $N_e = 807$. (b) $N_e = 1110$.

follow a normal distribution with mean value of 4 m and variance of 1.5 m. The generated fracture networks are shown in Fig. 10(a). The simplified fracture networks are shown in Fig. 10(b) after deleted unconnected cracks, which will not take part in grout fluid flow. Besides, the mechanical parameters of rock mass used in all the cases are same as those in section 4.1.

5.1. Mesh size

In this section, the effect of numerical model mesh size on the grout propagation depth is firstly investigated. The yield strength, viscosity, and initial fracture aperture are fixed as 3.0 Pa, 0.035 Pa s, and 3 mm, respectively. The initial grouting pressure is 0.5 MPa. The mesh size can

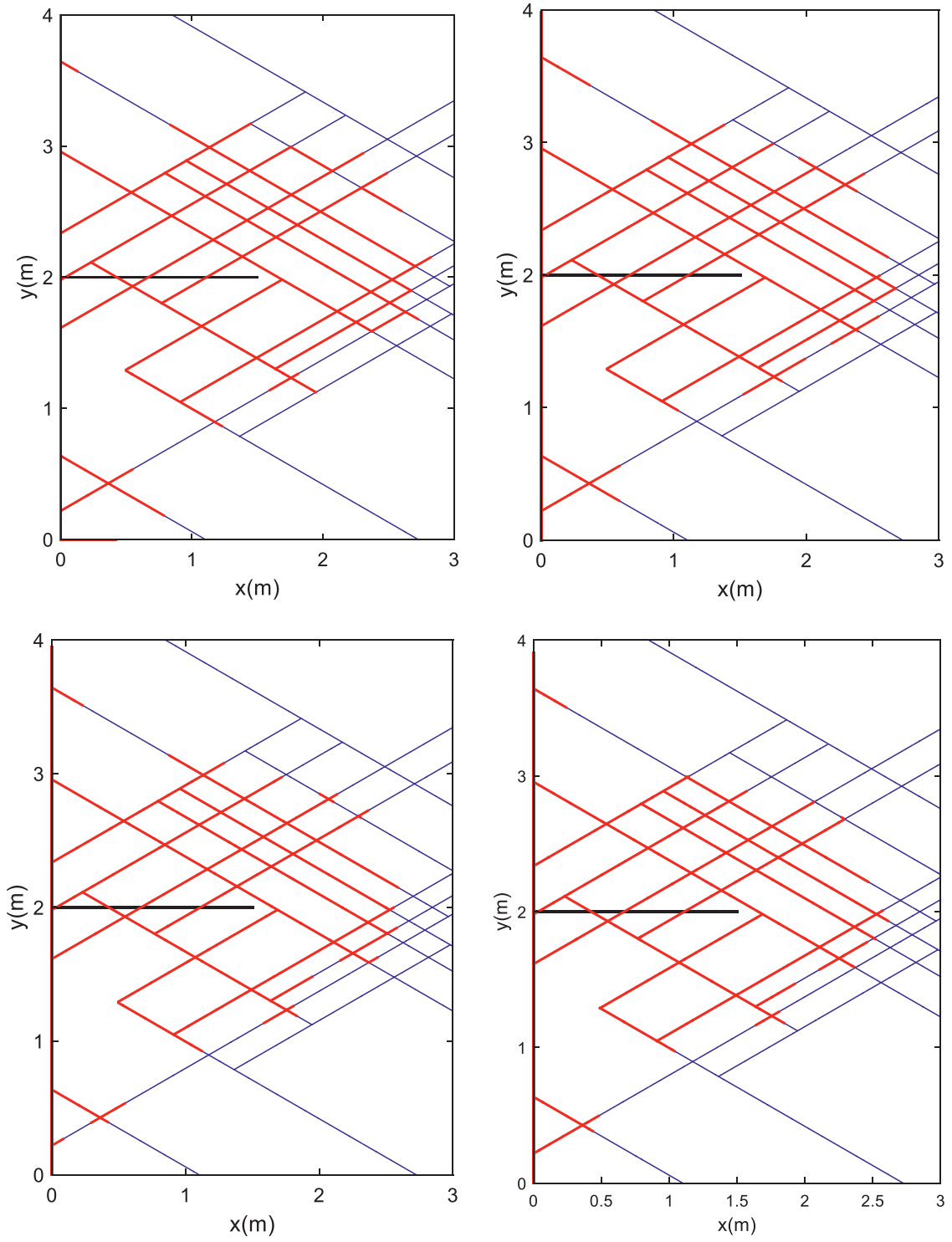

Fig. 12. Grouted zone distribution of different mesh sizes. (a) N_e = 216. (b) N_e = 544. (c) N_e = 807. (b) N_e = 1110.

be expressed by N_e (Number of MEs) and six different levels of N_e, i.e. 216, 369, 544, 807, 942, and 1110 are used in the numerical model respectively. As a result, the corresponding number of hydraulic nodes (N_n) are 218, 319, 410, 525, 586, 613, respectively. The typical meshes of numerical model are shown in Fig. 11.

Fig. 12 shows the final grouted zone of different level of mesh size. As illustrated in the figure, it is obviously that area if grouted zone decreases gradually as the number of MEs increases.

Further, Fig. 13 presents the curve of the grouting propagation depth with different level of mesh size. When the number of MEs is small, the grouting propagation depth is relatively high. With increasing of N_e, propagation depth rapidly decreases. After N_e reaches 800, the propagation depth decreases little and nearly keeps constant. As N_e increases from 807 to 1110, the propagation depth decreases from 29.614 m to 29.287 m. The results indicate that the grouting propagation depth firstly decreases quickly as the number of MEs increases and then it de-

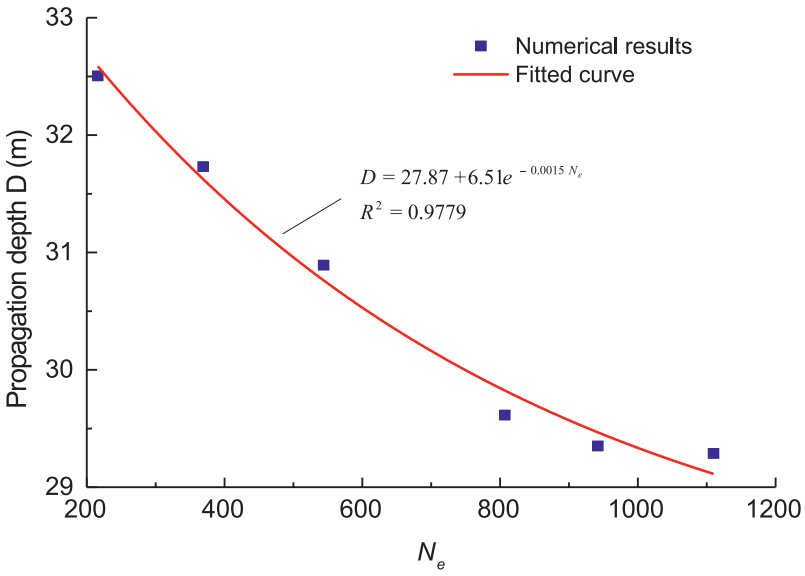

Fig. 13. Relationship between grouting propagation depth and number of MEs.

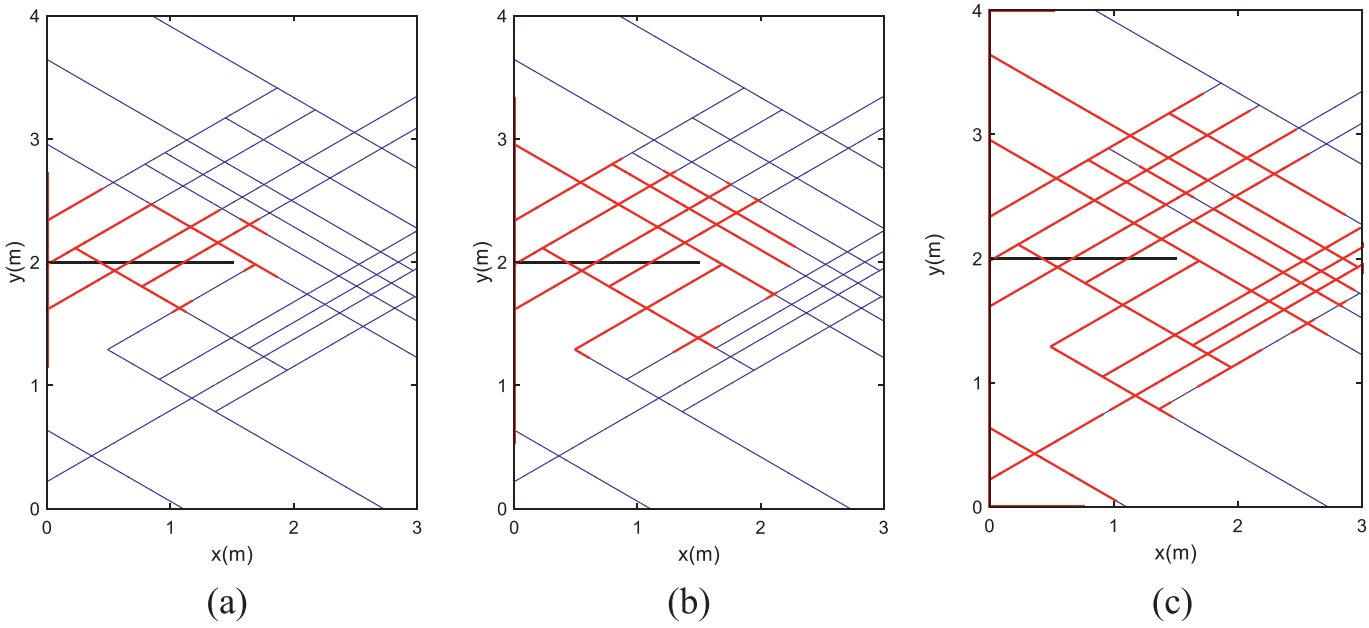

Fig. 14. Grouted zone distribution of different initial fracture apertures. (a) b = 1 mm. (b) b = 2 mm. (c) b = 4 mm.

creases very slowly when N_e overs a threshold. In this case, the threshold of N_e is 942, as a result, the N_e used in following numerical tests is 942.

5.2. Initial fracture aperture

The initial fracture aperture is also an important parameter affecting grouting zone in fractured rock mass. To investigate the effect of initial fracture aperture on grouting performance, in this section, six different values of initial fracture aperture b, i.e. 1.0 mm, 2.0 mm, 3.0 mm, 4.0 mm, 5.0 mm, and 6.0 mm are used in the numerical model respectively. The other parameters, including Bingham grout fluid and rock mechanics parameters are same as that used in section 5.1.

Fig. 14 shows some typical grouted zone distribution of different initial fracture apertures. As illustrated in the figure, the area of final grouted zone increases with the increase of fracture aperture obviously. Further, Fig. 15 presents the curve of the grouting propagation depth with initial fracture aperture. It is clearly that when b increases from 1 mm to 6 mm, the propagation depth increases from 8.505 m to 53.706 m. The linear fitting is also used and the fitted result shows that the propagation depth increases with increase of initial fracture aperture nearly linearly. The numerical results indicate that the increased initial fracture aperture will cause an increasing grouted area and depth, which can improve grouting effect.

5.3. Yield strength

In this section, the effect of yield strength on grouting in fractured rock mass is investigated. The viscosity and initial fracture aperture are fixed, and nine different values of yield strength, i.e. 3 Pa, 5 Pa, 8 Pa, 10 Pa, 15 Pa, 20 Pa, 25 Pa, 30 Pa, and 40 Pa, are adopted respectively in the study.

Fig. 16 shows some typical grouted zone distribution of different yield strength. As illustrated in the figure, the area of final grouted zone decreases with the increase of yield strength obviously. Further, Fig. 17 presents the curve of the grouting propagation depth with yield strength. The simulation results show that when τ_0 is low, the propagation depth

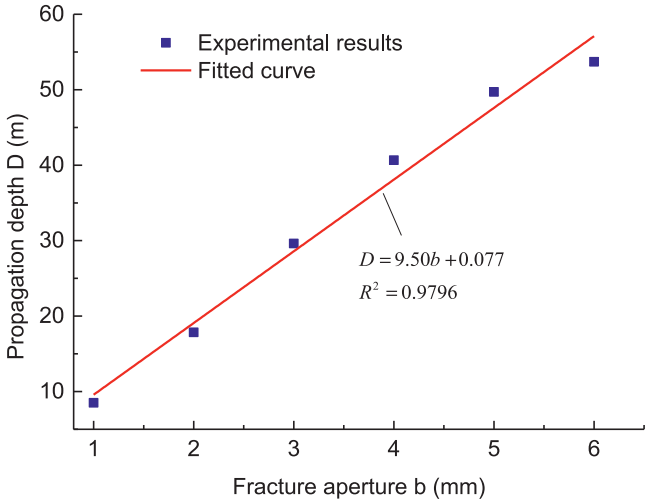

Fig. 15. Relationship between grouting propagation depth and initial fracture aperture.

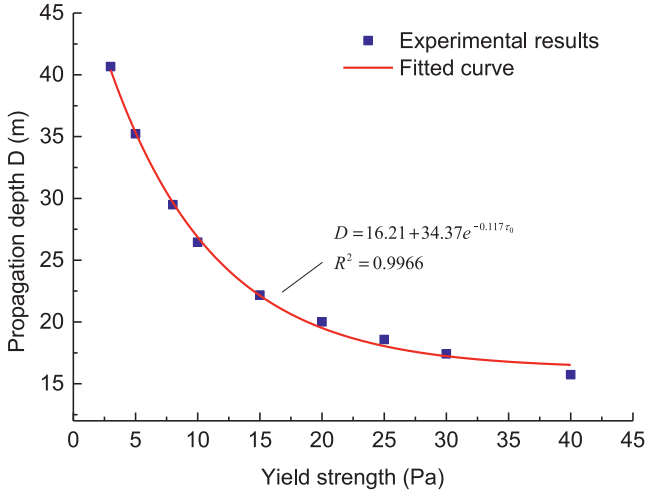

Fig. 17. Relationship between grouting propagation depth and yield strength.

is high. As τ_0 increases from 3 Pa to 15 Pa, the propagation depth decreases from 40.661 m to 22.174 m quickly. The decreasing rate is about 1.54 m/Pa. After τ_0 over 15 Pa, the propagation depth decreases from 20.011 m to 15.729 m with a decreasing rate of 0.21 m/Pa as τ_0 increases from 20 Pa to 40 Pa. Therefore, the numerical results indicate that the propagation depth nonlinearly decreases with increase of yield strength.

5.4. Initial grouting pressure

In this section, the effect of initial grouting pressure p_0 on grouting in fractured rock mass is investigated. The viscosity, initial fracture aperture and yield strength are fixed as 0.035 Pa s, 4 mm, and 20 Pa, respectively. Eleven different values of initial grouting pressure, i.e. 5000 Pa, 0.01 MPa, 0.05 MPa, 0.1 MPa, 0.3 MPa, 0.5 MPa, 0.6 MPa, 0.7 MPa, 0.8 MPa, 0.9 MPa and 1.0 MPa, are adopted respectively in the study.

Fig. 18 shows some typical grouted zone distribution of different initial grouting pressures. As illustrated in the figure, the area of final grouted zone increases with the increase of initial grouting pressure obviously. Further, Fig. 19 presents the curve of the grouting propagation depth with initial grouting pressure. It is clearly that when the propagation depth increases quickly from 1.178 m to 16.595 m when p_0 increases from 5000 Pa to 0.3 MPa. And then, the slope of the curve decreases gradually. Therefore, the numerical results indicate that the propagation depth increases nonlinearly as initial grouting pressure increases.

5.5. Discussion

According to the above numerical results, besides the simulation meshes, both the Bingham grout fluid and pre-existed crack properties have significant effects on the grouting performance in fractured rock masses. For the mesh size, as introduced in section 3, the minimum flowing distance in every time step depends on length of hydraulic line element. Once the grout fluid pressure gradient satisfied the criti-

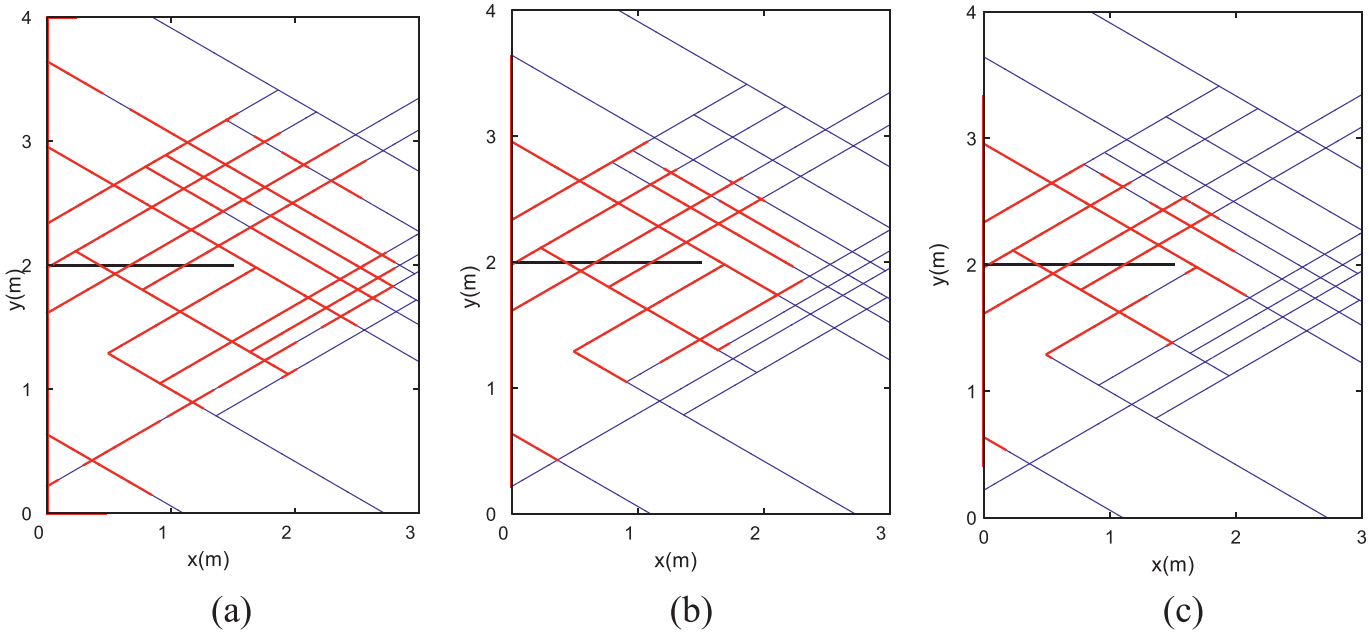

Fig. 16. Grouted zone distribution of different yield strength. (a) τ_0 = 5 Pa. (b) τ_0 = 20 Pa. (c) τ_0 = 40 Pa.

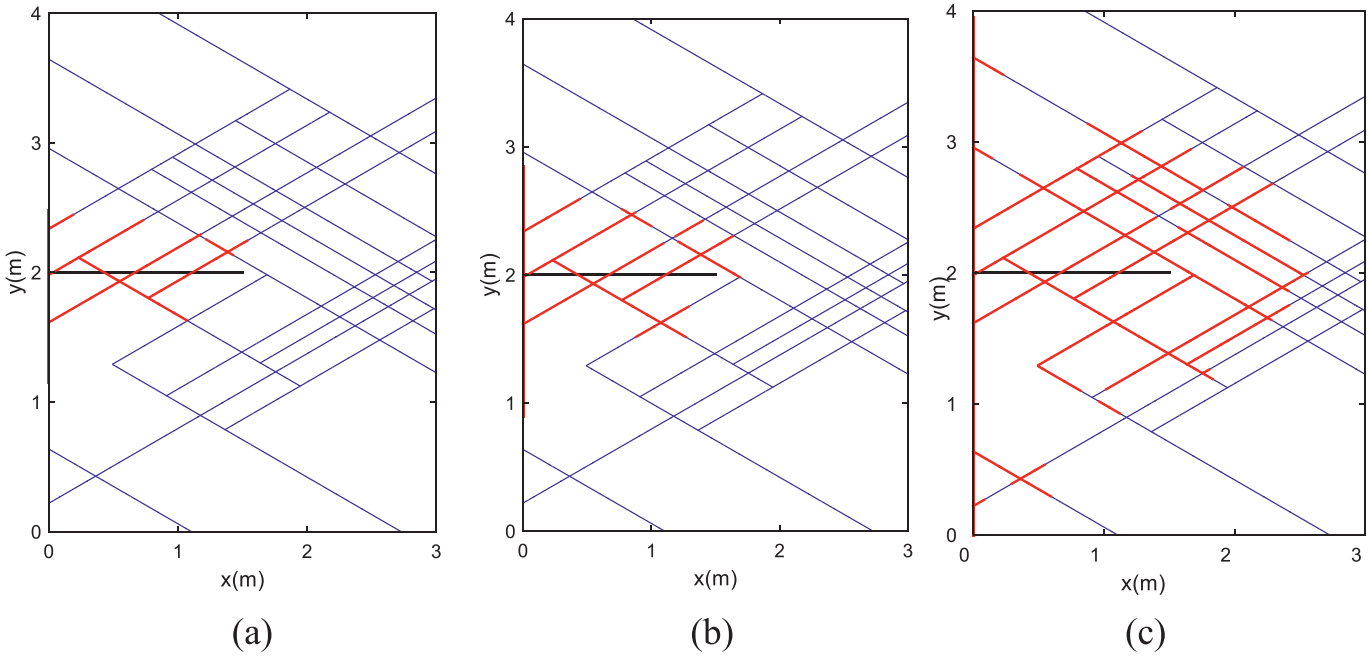

Fig. 18. Grouted zone distribution of different yield strength. (a) p_0 = 0.05 MPa. (b) p_0 = 0.1 MPa. (c) p_0 = 1.0 MPa.

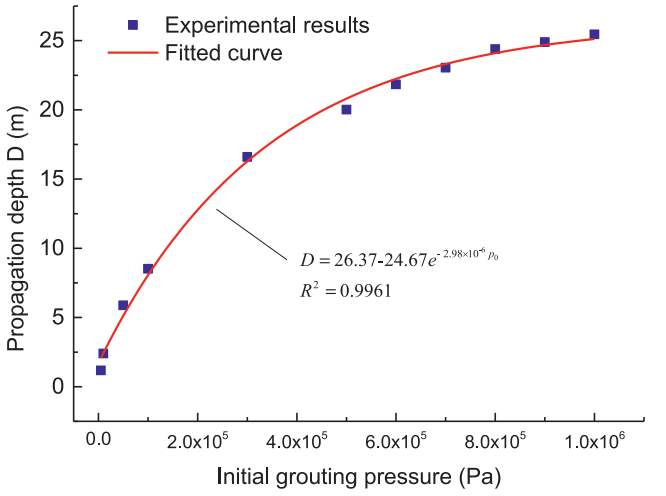

Fig. 19. Relationship between grouting propagation depth and initial grouting pressure.

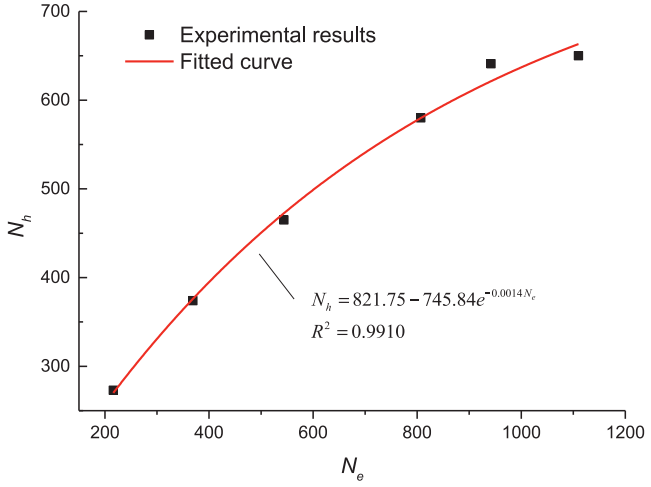

Fig. 20. Relationship between number of MEs and hydraulic line element.

cal pressure gradient in Eq. (11), the grout will fill up all the hydraulic line element. As a result, the number of line element (N_h) plays an important role in calculated grouting propagation depth during numerical simulation. Moreover, as shown in Fig. 20, the number of line element increases nonlinearly as the N_h increases. The fitting relationship indicates that the parameter N_h will finally reaches an unchanged value with the increase of N_e. At that time, the grouting propagation depth will no longer change as N_e changes.

The initial fracture aperture is a significant parameter during grouting. According to Eq. (13), for a fix grouting pressure, the flow rate increases as fracture aperture increases obviously. Besides, according to Eq. (11), the critical pressure gradient decreases as fracture aperture increases when yield strength is fixed. As a result, there will have more grout fluid flowing into more line elements and results in increasing of grouted zone area and propagation depth. Liu *et al.* [12] studied the in-situ effect of stress on grout penetration length using FDEM and found that the in-situ stress opens fractures and causes increasing of fracture aperture, and finally increases the penetration length. This result is consistent with the numerical tests results in this study.

Eriksson *et al.* [47] investigated the properties of cement grout and indicated that the yield strength decreases as W/C (water and cement) ratio increases. As we know, the smaller of W/C ratio, the more cement in the grout the poorer flowing ability of grout. As a result, a higher yield strength means a lower fluidity of grout slurry. Besides, similar to fracture aperture, according to Eq. (11), the critical pressure gradient increases as yield strength increases when fracture aperture is fixed. Therefore, When the yield strength of the slurry is high, the slurry becomes difficult to start flow and easy to stop flow.

6. Conclusions

In the study, an NMM grouting model, which is based on discrete fracture network model, is proposed to study grouting process in fractured rock mass. The global discretization equation, element submatrixes and NMM simulation algorithm are also presented. The pro-

posed NMM grouting method is verified and influence factors on the grouting performance are also investigated. The following conclusions can be drawn:

(1) In NMM grouting model, the grout fluid flowing behaviour is supposed as a Bingham fluid and only flows in the fractures and fluid governing equation is established by flow conservation. In DFN model, the hydraulic node and line element are the basic numerical calculation elements. For NMM, the line element information can be easily obtained and the number of line element are also enlarged during the generation of PCs and MEs, which is convenient and can improve the calculation accuracy. On basis of above, NMM simulation algorithm for grouting is finally proposed.
(2) The grouting in a single fracture and a regular fracture network numerical examples verified the effectiveness of the proposed NMM grouting model on simple and complex grouting process simulation by comparing with analytical solutions or experimental results.
(3) A parameter, namely propagation depth, is defined as the total length of hydraulic line elements where grout fluid arrived to evaluate grouting performance. Numerical tests indicated that the grouting propagation depth firstly decreases as number of MEs and yield strength increases, while the propagation depth increases as initial fracture aperture and grouting pressure increases.

Note that all the engineering problems under geostress and grouting process in fractured rock mass is a complex hydro-mechanical coupled process. Besides, the pressure on the fracture surfaces may cause the fracture propagation and connection. Only grout slurry flowing in fracture networks are considered in this study, the function of proposed NMM grouting model is limited. In future work, the NMM grouting model will be further improved, and be applied to solve fracture propagation under coupled hydro-mechanical and its influences on grouting

Declaration of Competing Interest

The authors declare no conflict of interest.

Acknowledgements

This work was supported by the National Nature Science Foundation of China [Grant NOs: 41807249, 51974289, and 51774267], Natural Science Foundation of Hubei Province (grant NO: 2019CFB535), and China Scholarship Council (Grant NO: 201804910219). The authors would also like to thank Professor Jian Zhao and Qianbing Zhang for valuable discussion, which inspired the authors to conduct the present research.

References

[1] Martino JB, Chandler NA. Excavation-induced damage studies at the underground research laboratory. Int J Rock Mech Min Sci 2004;41(8):1413–26.
[2] Du C, Cao P, Chen Y, Liu J, Zhao Y, Liu J. Study on the stability and deformation of the roadway subjected to high in-situ stresses. Geotech Geol Eng 2017;35(4):1–14.
[3] Seo HJ, Choi H, Lee IM. Numerical and experimental investigation of pillar reinforcement with pressurized grouting and pre-stress. Tunn Undergr Space Technol 2016;54:135–44.
[4] Gustafson G, Stille H. Prediction of groutability from grout properties and hydrogeological data. Tunn Undergr Space Technol 1996;11(3):325–32.
[5] Baca RG, Arnett RC, Langford DW. Modelling fluid flow in fractured porous rock masses by finite element techniques. Int J Numer Methods Fluids 1984;4(4):337–48.
[6] Prevost JH, Sukumar N. Faults simulations for three-dimensional reservoir-geomechanical models with the extended finite element method. J Mech Phys Solids 2016;86:1–8.
[7] Saeidi O, Stille H, Torabi SR. Numerical and analytical analyses of the effects of different joint and grout properties on the rock mass groutability. Tunn Undergr Space Technol 2013;38:11–25.
[8] Eriksson M, Stille H, Andersson J. Numerical calculations for prediction of grout spread with account for filtration and varying aperture. Tunn Undergr Space Technol 2000;15(4):353–64.
[9] Xiao F, Shang J, Zhao Z. DDA based grouting prediction and linkage between fracture aperture distribution and grouting characteristics. Tunn Undergr Space Technol 2019;112:350–69.
[10] Mohajerani S, Baghbanan A, Bagherpour R, Hashemolhosseini H. Grout penetration in fractured rock mass using a new developed explicit algorithm. Int J Rock Mech Min Sci 2015;80:412–17.
[11] Liu QS, Sun L. Simulation of coupled hydro-mechanical interactions during grouting process in fractured media based on the combined finite-discrete element method. Tunn Undergr Space Technol 2019;84:472–86.
[12] Liu QS, Sun L, Tang XH. Investigate the influence of the in-situ stress conditions on the grout penetration process in fractured rocks using the combined finite-discrete element method. Eng Anal Bound Elem 2019;106:86–101.
[13] Sun L, Grasselli G, Liu QS, Tang XH. Coupled hydro-mechanical analysis for grout penetration in fractured rocks using the finite-discrete element method. Int J Rock Mech Min Sci 2019;124:104138.
[14] Fan LF, Yi XW, Ma GW. Numerical manifold method (NMM) simulation of stress wave propagation through fractured rock mass. Int J Appl Mech 2013;5(2):238–49.
[15] Liu F, Zhang K, Liu Z. Three-dimensional MLS-based numerical manifold method for static and dynamic analysis. Eng Anal Bound Elem 2019;109:43–56.
[16] Liu F, Yu CY, Yang YT. An edge-based smoothed numerical manifold method and its application to static, free and forced vibration analyses. Eng Anal Bound Elem 2018;86:19–30.
[17] Wong LNY, Wu ZJ. Application of the numerical manifold method to model progressive failure in rock slopes. Eng Fract Mech 2014;119:1–20.
[18] Zhang HH, Ma GW, Fan LF. Thermal shock analysis of 2D cracked solids using the numerical manifold method and precise time integration. Eng Anal Bound Elem 2017;75:46–56.
[19] Zhang HH, Ma GW, Ren F. Implementation of the numerical manifold method for thermo-mechanical fracture of planar solids. Eng Anal Bound Elem 2014;44:45–54.
[20] He J, Liu QS, Wu ZJ. Creep crack analysis of viscoelastic material by numerical manifold method. Eng Anal Bound Elem 2017;80:72–86.
[21] Yang YT, Tang XH, Zheng H, Liu QS, Liu ZJ. Hydraulic fracturing modeling using the enriched numerical manifold method. Appl Math Model 2018;53:462–86.
[22] Wu ZJ, Xu XY, Liu QS, Yang YT. A zero-thickness cohesive element-based numerical manifold method for rock mechanical behavior with micro-Voronoi grains. Eng Anal Bound Elem 2018;96:94–108.
[23] Liu XW, Liu QS, He J, Yu FZ. Numerical simulation of cracking process in rock mass under the coupled thermo-mechanical condition. Int J Comput Methods 2020;17(9):1950065.
[24] Yang YT, Guo HW, Fu XD, Zheng H. Boundary settings for the seismic dynamic response analysis of rock masses using the numerical manifold method. Int J Numer Anal Methods Geomech 2018;42(9):1095–122.
[25] Wei W, Zhao Q, Jiang QH, Grasselli G. Three new boundary conditions for the seismic response analysis of geomechanics problems using the numerical manifold method. Int J Rock Mech Mining Sci 2018;105:110–22.
[26] Liu XW, Liu QS, Wei L, Huang X. Improved strength criterion and numerical manifold method for fracture initiation and propagation. Int J Geomech 2016;17(5):E4016007.
[27] Liu XW, Liu QS, He J, Liu B. Modified contact model with rock joint constitutive in numerical manifold method. Eng Anal Bound Elem 2018;93:63–71.
[28] Liu XW, Liu QS, Liu B, He J. Numerical manifold method for thermal–hydraulic coupling in fractured enhance geothermal system. Eng Anal Bound Elem 2019;101:67–75.
[29] Wu ZJ, Liang X, Liu QS. Numerical investigation of rock heterogeneity effect on rock dynamic strength and failure process using cohesive fracture model. Eng Geol 2015;197:198–210.
[30] Yang YT, Tang XH, Zheng H, Liu QS, He L. Three-dimensional fracture propagation with numerical manifold method. Eng Anal Bound Elem 2016;72:65–77.
[31] Fan LF, Zhou XF, Wu ZJ. Investigation of stress wave induced cracking behavior of underground rock mass by the numerical manifold method. Tunn Undergr Sp Tech 2019;92:103032.
[32] Liu TT, Li XP, Zheng Y, Luo Y, Guo YH, Cheng GW, Zhang ZZ. Study on S-wave propagation through parallel rock joints under in situ stress. Wave Random Complex 2020. doi:10.1080/17455030.2020.1813350.
[33] Hu MS, Rutqvist J. Microscale mechanical modeling of deformable geomaterials with dynamic contacts based on the numerical manifold method. Computat Geosci 2020;24:1783–97.
[34] Wu ZJ, Fan LF, Liu QS, Ma GW. Micro-mechanical modeling of the macro-mechanical response and fracture behavior of rock using the numerical manifold method. Eng Geol 2017;225(20):49–60.
[35] Hu MS, Rutqvist J. Numerical manifold method modeling of coupled processes in fractured geological media at multiple scales. J Rock Mech Geotech 2020;12(4):667–81.
[36] Zheng H, Liu F, Li C. Primal mixed solution to unconfined seepage flow in porous media with numerical manifold method. App Math Model 2015;39(2):794–808.
[37] Hu MS, Rutqvist J, Wang Y. A practical model for fluid flow in discrete-fracture porous media by using the numerical manifold method. Adv Water Resour 2016;97:38–51.
[38] Hu MS, Rutqvist J, Wang Y. A numerical manifold method model for analyzing fully coupled hydro-mechanical processes in porous rock masses with discrete fractures. Adv Water Resour 2017;102:111–26.
[39] Ma GW, Wang HD, Fan LF, Chen Y. Segmented two-phase flow analysis in fractured geological medium based on the numerical manifold method. Adv Water Resour 2018;121:112–29.

[40] Ma GW, Wang HD, Fan LF, Chen Y. A unified pipe-network-based numerical manifold method for simulating immiscible two-phase flow in geological media. J Hydrol 2019;568:119–34.
[41] Yang MJ, Yue ZQ, Lee PK, Su B, Tham LG. Prediction of grout penetration in fractured rocks by numerical simula. Canad Geotech J 2002;39(6):1384–94.
[42] Wallner M. Propagation of sedimentation stable cement pastes in jointed rock. Rock Mech Waterw Constr 1976;2:132–6.
[43] Amadei B, Savage WZ. An analytical solution for transient flow of Bingham viscoplastic materials in rock fractures. Int J Rock Mech Mining Sci 2001;38(2):285–96.
[44] Hassler L, Hakansson U, Stille H. Computer-simulated flow of grouts in jointed rock. Tunn Undergr Space Technol 1992;7(4):441–6.
[45] Hakansson UM. Icke-newtonsk strömning i endimensionella kanaler Master Thesis. Stockholm, Sweden: Department of Civil and Environmental Engineering, KTH Royal Institute of Technology; 1987.
[46] Zhang QS, Zhang LZ, Liu RT, Li SC, Zhang QQ. Grouting mechanism of quick setting slurry in rock fissure with consideration of viscosity variation with space. Tunn Undergr Space Technol 2017;70:262–73.
[47] Eriksson M, Friedrich M, Vorschulze C. Variations in the rheology and penetrability of cement-based grouts—an experimental study. Cem Concr Res 2004;34(7):1111–19.